Chinese Chemical Letters 35 (2024) 108450

Contents lists available at ScienceDirect

Chinese Chemical Letters

journal homepage: www.elsevier.com/locate/cclet

Copper-induced formation of heterostructured Co_3O_4/CuO hollow nanospheres towards greatly enhanced lithium storage performance

Junjun Zhang[a,1], Huiying Lu[b,1], Tianhao Yao[b], Xin Ji[b], Qingmiao Zhang[c], Lingjie Meng[c], Jianmin Feng[a], Hongkang Wang[b,*]

[a] College of Geography & Environment, Xianyang Normal University, Xianyang 712000, China
[b] State Key Lab of Electrical Insulation and Power Equipment, Center of Nanomaterials for Renewable Energy (CNRE), School of Electrical Engineering, Xi'an Jiaotong University, Xi'an 710049, China
[c] School of Chemistry, Xi'an Key Laboratory of Sustainable Energy Material Chemistry, and Instrumental Analysis Center, Xi'an Jiaotong University, Xi'an 710049, China

ARTICLE INFO

Article history:
Received 30 January 2023
Revised 23 March 2023
Accepted 12 April 2023
Available online 14 April 2023

Keywords:
Lithium-ion batteries
Co/Cu-glycerate
Hollow nanospheres
Co_3O_4/CuO heterostructure
Electrochemical properties

ABSTRACT

We report a facile template-free fabrication of heterostructured Co_3O_4/CuO hollow nanospheres using pre-synthesized Co/Cu-glycerate as conformal precursor. The introduction of copper nitrate in the solvothermal reaction system of glycerol/isopropanol/cobalt nitrate readily induces the conversion from solid Co-glycerate to hollow Co/Cu-glycerate nanospheres, and the effect of the Co/Cu atomic ratio on the structure evolution of the metal glycerates as well as their corresponding oxides were investigated. When examined as anode materials for lithium-ion batteries, the well-defined Co_3O_4/CuO hollow nanospheres with Co/Cu molar ratio of 2.0 demonstrate excellent lithium storage performance, delivering a high reversible capacity of 930 mAh/g after 300 cycles at a current density of 0.5 A/g and a stable capacity of 650 mAh/g after 500 cycles even at a higher current density of 2.0 A/g, which are much better than their counterparts of bare CuO and Co_3O_4. The enhanced lithium storage performance can be attributed to the synergistic effect of the CuO and Co_3O_4 heterostructure with hollow spherical morphology, which greatly enhances the charge/electrolyte transfer and effectively buffers the volume changes upon lithiation/delithiation cycling.

Lithium-ion batteries (LIBs) have been considered as one of the most promising electrochemical energy storage devices owing to their high energy/power density, environmental friendliness and long lifespan [1–7]. However, with the increasing demand for higher energy density and better safety in large-scale energy storage fields such as electric vehicles and smart-grid, the current graphite anode of commercial LIBs could not meet these requirements due to its lower theoretical capacity (372 mAh/g) and the safety problem arising from the lithium dendrite in the low working potential (*vs.* Li/Li^+) [8–12]. Therefore, it is highly desired to explore high-performance anode materials for next-generation LIBs.

As a kind of promising alternative anode for LIBs, transition metal oxides (TMOs) have received considerable attention owing to their high theoretical capacities, abundant reserve, high safety and affordable cost [13–15]. Especially, Co_3O_4 (890 mAh/g) and CuO (674 mAh/g) have attracted many interests because of their high theoretical capacities, easy preparation and wide availability [16–19]. Nevertheless, the poor electrical conductivity and large volume expansion hinder their practical application, as the large volume changes upon lithiation/delithiation processes usually lead to electrode pulverization and thus resulting in fast capacity fading with poor cycling stability, while the poor electrical conductivity would result in the unsatisfied rate capability [20]. To address these drawbacks, nanostructure engineering with dimensional/morphological control and heterostructure construction has been widely adopted, as the well-designed nanostructures, such as nanofibers, nanosheets and nanospheres with hollow/porous interiors, could efficiently shorten the lithium-ion diffusion paths, expose more ion storage sites, and facilitate the fast electron/ion transport [21,22]. For instance, Wang *et al.* fabricated hollow Co_3O_4 nanoparticle-assembled nanofibers *via* electrospinning and subsequent annealing, which displayed excellent cycle stability of ~871.5 mAh/g after 500 cycles at 0.2 A/g [23]. Ji *et al.* developed a porous

* Corresponding author.
E-mail address: hongkang.wang@mail.xjtu.edu.cn (H. Wang).
[1] These authors contributed equally to this work.

https://doi.org/10.1016/j.cclet.2023.108450
1001-8417/

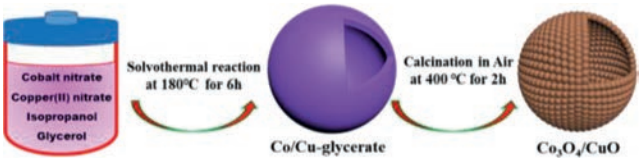

Fig. 1. Schematic illustration of the fabrication processes of the Co/Cu-glycerate and the resulting Co_3O_4/CuO hybrid with conformal hollow spherical morphology.

hollow carbon scaffold to anchor ultrafine Co_3O_4 nanoparticles, which showed enhanced cycling stability and lithium storage capacity compared to bare Co_3O_4 [24].

Heterostructured hybrid electrodes consisting of different active materials usually exhibit enhanced reaction kinetics, which could efficiently improve the electrochemical performance [25,26]. To date, various Co_3O_4/CuO hybrids with well-defined microstructures have been developed to enhance their lithium storage performance by virtue of their synergistic enhancement effect of the two components. For example, Wu *et al.* designed and prepared graphene quantum dots modified yolk-shell Co_3O_4@CuO microspheres, which displayed a high reversible capacity of 1054 mAh/g after 200 cycles at 0.1 A/g [27]. Wang *et al.* prepared heterostructured core/shell arrays of Co_3O_4 nanosheets decorated CuO nanowire on nickel foam, which demonstrated good cycle performance and high reversible capacity (1191 mAh/g with 90.9% capacity retention after 200 cycles at 0.2 A/g) and excellent rate capability (810 mAh/g after 500 cycles at 1 A/g) [28]. Even though greatly enhanced lithium storage performances have been achieved, these fabrication processes are complicated and not easy for scale-up production. Herein, we developed a facile one-pot route to synthesize hollow Co_3O_4/CuO nanospheres by using solvothermally prepared Co/Cu-glycerate as conformal precursor and studied the effect of Co/Cu atomic ratio on the microstructure evolution of the metal glycerates and their derivate oxides obtained by calcination method. When investigated as an anode material for LIBs, the hollow Co_3O_4/CuO nanospheres displayed excellent lithium storage performance including high reversible capacity, outstanding cycling stability and superior rate capability (930 mAh/g after 300 cycles at 0.5 A/g and 650 mAh/g after 500 cycles even at 2.0 A/g), which is owing to the unique hollow heterogeneous nanostructure.

Fig. 1 illustrates the formation of hollow Co/Cu-glycerate and the derivate Co_3O_4/CuO nanospheres, which are prepared *via* solvothermal method with subsequent calcination treatment (see more details in Supporting information). Typically, $Co(NO_3)_2{\cdot}6H_2O$ and $Cu(NO_3)_2{\cdot}2.5H_2O$ are dissolved in the mixture solution of isopropanol and glycerol, serving as precursor solution which is encapsulated in a Teflon vessel and reacted at 180 °C for 6 h. In this process, the Cu^{2+}/Co^{2+} metal ions are complexed with organic ligands through metal–hydroxyl interaction, forming uniform Co/Cu glycerate hollow nanospheres. As revealed by the thermogravimetric analysis (TGA), the Co/Cu-glycerate is thermally unstable and shows abrupt decomposition at around 260 °C with a total weight loss of ~36.3 wt% (Fig. S1a in Supporting information), suggesting the organic component undergoes complete and fast combustion into gaseous species. Even further increasing the testing temperature, the weight still keeps constant and the residual is confirmed as Co_3O_4/CuO hybrid (Fig. S1b in Supporting information).

To verify the effect of Cu ions on the formation of the hollow spherical structure, pure Co and Co/Cu ions were reacted with glycerol under solvothermal condition, forming spherical Co-glycerate with solid interiors and Co/Cu glycerate with hollow interiors, suggesting the introduction of Cu ions induce the formation of well-defined hollow nanospheres, which will be in favor of enhanced charge transferability and cycling stability. Fig. 2a shows the scanning electron microscope (SEM) image of the Co-glycerate spheres, which display an average diameter of around 500 nm with smooth surface. Fig. 2b shows the high-angle annular dark field (HAADF) scanning transmission electron microscopy (STEM) image of a single Co-glycerate sphere with solid structure, in which the Co and O elements are well distributed and overlapped within the sphere (Figs. 2c and d). Interestingly, when substituting part of Co ions with Cu ions, the solid-to-hollow evolution is observed. As shown in Figs. 2e and f, the as-prepared Co/Cu glycerate with Co/Cu molar ratio of 2.0 shows well-defined monodispersed hollow spherical morphology, and the hollow Co/Cu glycerate spheres show an average diameter of around 500 nm and a shell thickness of around 100 nm but with rough surface, which is composed of downy species. In addition, the corresponding elemental energy-dispersive X-ray spectrometer (EDS) maps of the single Cu/Co-glycerate sphere intuitively illustrate the well-overlapped distribution of Cu and Co, indicating the uniform formation of the Co/Cu-glycerol complex (Figs. 2g and h). Moreover, Table S1 (Supporting information) compares the structure evolution upon varying the molar ratio of Co/Cu. Note that the pure Cu-glycerate displays irregular aggregate morphology, which consists of randomly packed nanoparticles. With increasing the Co/Cu molar ratio from 0.5 to 1.0, the as-prepared Co/Cu-glycerates show hollow spherical morphology but with poor uniformity and broken/opened structure. These results demonstrate that the Co-glycerol complex is prone to form spherical aggregation, while the Cu-glycerol complex would preferentially aggregate loosely, thus the synergistic interaction of Co-Cu ions and glycerol induces the hollowing of the Co/Cu-glycerate.

The metal-glycerol complex can be an ideal conformal template to synthesize the oxide counterpart, and the bare Co, Cu

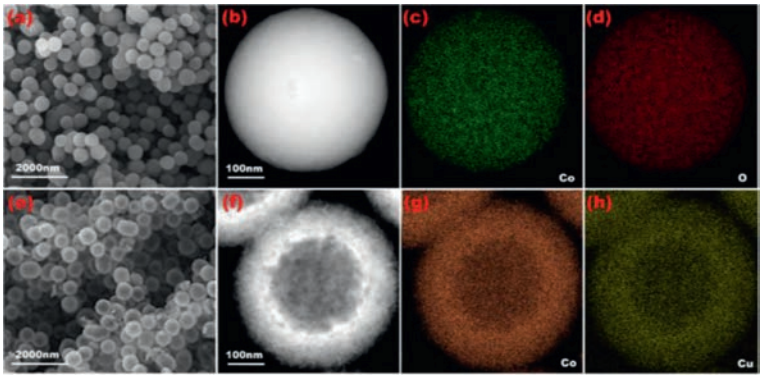

Fig. 2. (a) SEM and (b) HAADF STEM images of the Co glycerate precursor with corresponding EDS maps of (c) Co and (d) O elements. (e) SEM and (f) HAADF STEM images of Co/Cu glycerate precursor with corresponding EDS maps of (g) Co and (h) Cu elements.

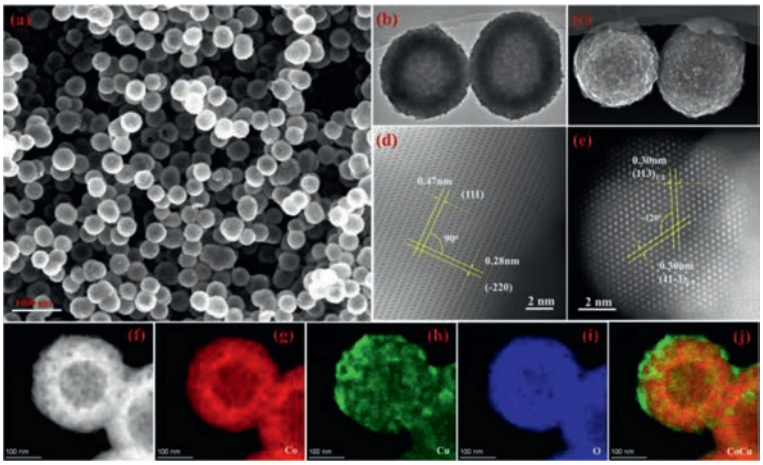

Fig. 3. (a) SEM, (b) TEM and (c) STEM images of the Co_3O_4/CuO hollow spheres. HRTEM images taken at different areas showing the lattice fringes of (d) Co_3O_4 and (e) CuO. (f) HAADF STEM image of a single hollow sphere with corresponding EDS maps of (g) Co, (h) Cu, (i) O and (j) the overlapping map of Co/Cu elements.

and various Co/Cu glycerates readily converted into oxide phases with almost the same morphology (Table S1 and Fig. 3). Fig. 3a shows the SEM image of the well-defined Co_3O_4/CuO hollow spheres with uniform diameter and monodispersing. The transmission electron microscope (TEM) image reveals the hollow spheres show a shell thickness of ~80 nm, which is composed of densely packed nanoparticles (Figs. 3b and c). Figs. 3d and e show the high-resolution TEM (HRTEM) images with different lattice fringes, which can be ascribed to the Co_3O_4 and the CuO, respectively. In Fig. 3d, two sets of lattice fringes show *d*-spacings of 0.47 and 0.28 nm, which are correspondingly indexed to the (111) and $(\bar{2}20)$ planes of cubic Co_3O_4 (JCPDS No. 43–1003) with an angle of 90° [29,30], consistent with the theoretical value. Fig. 3e shows another two sets of lattice fringes with the same d spacing of 0.30 nm and an angle of around 120°, which can be well ascribed to the $(113)_{1/2}$ and $(11\bar{3})_{1/2}$ of monoclinic CuO (JCPDS No. 48–1548) [31]. Note that the $(113)_{1/2}$ and $(11\bar{3})_{1/2}$ reflect the 1/2 positions of (113) and $(11\bar{3})$ which is two times as much as that of (113) plane [32]. Fig. 3f shows the HAADF STEM image of a single hollow sphere, whose EDS maps are correspondingly shown in Figs. 3g-j. It is noteworthy that the Co and O elements are well overlapped, while accumulation of Cu element can be observed, suggesting the phase separation of Co_3O_4 and CuO to some extent.

X-ray diffraction (XRD) measurements were also conducted to verify the phase structure of the products. As shown in Fig. S2a (Supporting information), the products prepared with single metal source show typical diffraction peaks of Co_3O_4 (JCPDS No. 43–1003) and CuO (JCPDS No. 48–1548), respectively, suggesting their pure phase. Fig. S2b (Supporting information) depicts the XRD patterns of Co_3O_4/CuO with different molar ratios, where the typical peaks for both Co_3O_4 and CuO can be detected, suggesting their hybrid structure. As the Co/Cu molar ratio gradually decreases from 2/1 to 1/2, the peaks at 31.3° and 36.8° (Co_3O_4) become weaker, and the typical peaks for CuO (35.5° and 38.7°) become much more prominent, which is in good agreement with the content ratio in preparation.

The chemical compositions and oxidation states of the as-prepared Co_3O_4/CuO hollow spheres were revealed by X-ray photoelectron spectroscopy (XPS) analysis, and the survey spectrum clearly indicates the presence of Co, Cu and O elements (Fig. S3a in Supporting information). As shown in the high-resolution Co 2p XPS spectrum (Fig. S3b in Supporting information), two prominent peaks at 779.7 and 794.6 eV are typically assigned to the Co $2p_{3/2}$ and Co $2p_{1/2}$ of the Co_3O_4 phase, respectively. In addition, two shake-up satellite peaks ("Sat") appear at 789.4 and 803.6 eV. The Co 2p spectrum can be further fitted into two spin-orbit doublets, in which the peaks at around 779.7 and 794.6 eV are ascribed to Co^{3+}, while the peaks at 781.9 and 796.6 eV relate to Co^{2+} [33–36]. Fig. S3c (Supporting information) shows the Cu 2p XPS spectrum, in which the two peaks at 933.9 and 953.5 eV are correspondingly assigned to the Cu $2p_{3/2}$ and Cu $2p_{1/2}$, while three fitted satellite peaks appear at 941.0, 943.4 and 961.8 eV, indicating the oxidation state of Cu^{2+} as CuO in the hybrid [37,38]. In the O 1s XPS spectrum (Fig. S3d in Supporting information), three characteristic peaks can be fitted and located at 529.6, 531.2 and 532.9 eV, which can be ascribed to metal-oxygen bonds, the lattice oxygen, and the surface oxygen originated from the physically/chemically adsorbed water, respectively [39].

To verify the efficacy of the Co_3O_4/CuO heterostructure as anode for LIBs, the lithium storage properties of Co_3O_4, CuO and various Co_3O_4/CuO were examined in half-cells using lithium metal as counter/reference electrode. Cyclic voltammograms (CV) were performed to investigate the lithium storage mechanism, and Fig. 4a shows the typical CV curves of Co_3O_4/CuO for the first five cycles at 0.2 mV/s. In the first cathodic scan, three peaks are observed, and the minor cathodic peaks at 1.64 V can be attributed to the reduction of CuO into Cu_2O [40], while the prominent peak at 0.96 V accompanied by a minor peak at 0.70 V can be ascribed to the reduction of Co_3O_4 into Co and reduction of Cu_2O into Cu, as well as the formation of solid electrolyte interface (SEI) film [41,42], in which the prominent peak at 0.96 V disappears in the following cycles, indicating the irreversible capacity loss owing to the structure destruction and the formation of SEI film [43,44]. In the following four cycles, two newly merged cathodic peaks steadily appear at 0.92/1.16 V, corresponding to the highly reversible reduction of the Co/Cu oxides. In the anodic sweep, a broad peak at 2.07 V can be attributed to the oxidation of the metallic Cu and Co to CuO and Co_3O_4, respectively [45,46]. The anodic peak in the following cycles remains similar, suggesting good reversibility for the redox reaction. Moreover, the CV curves for the bare Co_3O_4 and CuO are provided in Fig. S4 (Supporting information), and the Co_3O_4/CuO electrode displays a smaller potential difference (0.94 V) between the anodic/cathodic peaks (ΔE) than those for the bare Co_3O_4 (1.07 V) and the bare CuO (1.34 V) electrodes (Fig. 4b), suggesting the faster kinetics of Co_3O_4/CuO [47].

Fig. 4c shows the galvanostatic discharge/charge profiles of the Co_3O_4/CuO electrode at different cycles at 0.2 A/g. The first discharge/charge capacities are 1900/1058 mAh/g with an initial

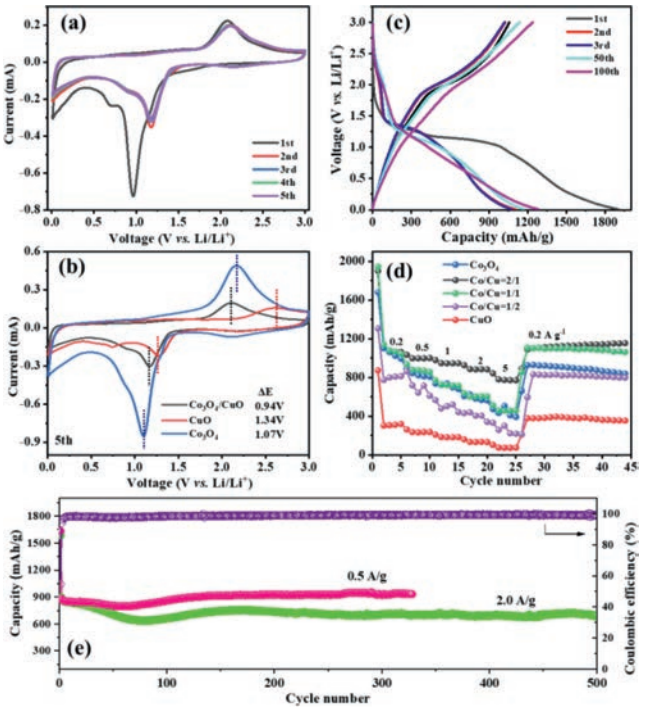

Fig. 4. (a) CV curves of the Co_3O_4/CuO electrode for the first five cycles at 0.2 mV/s, and (b) comparison of the 5th CV curves for the CuO, Co_3O_4 and Co_3O_4/CuO electrodes. (c) Galvanostatic discharge/charge profiles of the Co_3O_4/CuO electrode at 0.2 A/g. (d) Rate performance at different current densities for the CuO, Co_3O_4 and Co_3O_4/CuO electrodes with different Co/Cu molar ratios. (e) Cycle performances of the optimized Co_3O_4/CuO electrode at 0.5 and 2.0 A/g.

Coulombic efficiency (CE) of 55.7%. The capacity loss in the first cycle is due to the reversible formation of SEI film [48]. In the 2nd/3rd cycles, the CEs increase to 93.0%/95.0%, indicating the gradually increased reversibility of the redox reaction. With further increasing the cycling to the 50th and 100th cycles, the charge/discharge capacities increase, which is consistent with the rate test. Fig. 4d displays the rate performance of the CuO, Co_3O_4 and Co_3O_4/CuO electrodes with different Co/Cu molar ratios with current densities ranging from 0.2 A/g to 5.0 A/g, among which the Co_3O_4/CuO (Co/Cu = 2/1) demonstrates the highest lithium storage capacity, delivering high reversible capacities of 1023, 974, 930, 870 and 760 mAh/g each after 5 cycles at 0.2, 0.5, 1.0, 2.0 and 5.0 A/g, respectively. When cycling again at 0.2 A/g, the Co_3O_4/CuO (Co/Cu = 2/1) electrode shows steadily increased reversible capacity, delivering a high discharge capacity of 1156 mAh/g after another 20 cycles. However, the pure Co_3O_4 and Co_3O_4/CuO (Co/Cu = 1/1 and 1/2) electrodes suffer from capacity fading as the current increases, suggesting their poor rate capability. It is worth noting that the initial capacity of the Co_3O_4/CuO electrodes shows a downward trend as the Co concentration decreases, as the Co_3O_4 counterpart would offer more theoretical capacity than that for CuO. Interestingly, the Co_3O_4/CuO (Co/Cu = 2/1 and 1/1) almost show similar initial capacity compared to pure Co_3O_4 electrode, which suggests that the heterostructured Co_3O_4/CuO with hollow structure would provide more lithium storage sites. In contrast, the pure CuO electrode displays the worst cycle and rate performances with the lowest discharge capacity of 390 mAh/g at 0.2 A/g and only 50 mAh/g at 5.0 A/g. Furthermore, Fig. S5 (Supporting information) compares the cycling performances of the CuO, Co_3O_4 and Co_3O_4/CuO electrodes with different Co/Cu molar ratios at high current density, displaying the trend of descending in the initial cycles and then ascending, which can be seen in most transition metal oxide electrodes. The phenomena with continuous capacity increase can be widely observed in the transition metal-based anodes, which was generally attributed to the continuous activation of the electrode materials and the reversible formation/decomposition of electrolyte-derived surface layer, thus bringing additional charge storage capacity [49,50]. When cycling at 0.5 A/g (Fig. 4e), the Co_3O_4/CuO electrode exhibits a high reversible capacity of 883.5 mAh/g in the 2nd cycle and then the lowest capacity of 797.5 mAh/g at the 57th cycle, which may be due to the formation of thick SEI layer that retards electron transport and extends the diffusion length for lithium ions [31,51,52]. In the subsequent cycles, the capacity increases to 938.6 mAh/g with a capacity retention of 106.2% after 300 cycles. Even cycling at 2.0 A/g (Fig. 4e), the discharge capacity retains 693.4 mAh/g after 500 cycles, which is higher than most of other previously reported Co_3O_4 or CuO-based anodes (Table S2 in Supporting information). Electrochemical impedance spectroscopy (EIS) measurements were also conducted to reveal the charge transfer kinetics of these electrodes, which clearly reveals that the Co_3O_4/CuO electrode exhibits the smallest charge transfer resistance (R_{ct}) of 71.4 Ω (Fig. S6 and Table S3 Supporting information), as compared with the CuO (109.1 Ω) and Co_3O_4 (267.4 Ω) electrodes.

The structural stability of the hollow Co_3O_4/CuO nanospheres upon lithiation/delithiation cycling was also examined by *ex-situ* TEM analysis (Fig. S7 in Supporting information), revealing that the hollow spherical shape of the discharged and charged Co_3O_4/CuO electrode in the initial cycle is well preserved, even after 300 cycles at 0.5 A/g. In addition, EDS maps clearly display that the Co and Cu elements are uniformly distributed and well overlapped with the discharged/charged Co_3O_4/CuO. These results demonstrate that the hollow Co_3O_4/CuO heterostructure can efficiently buffer the volume changes upon cycling, indicating its robust structure stability as an anode material for LIBs.

In summary, we demonstrated a facile way to construct heterostructured Co_3O_4/CuO with well-defined hollow spherical morphology, using the solvothermally pre-synthesized Co/Cu-glycerate as the conformal template. The introduction of Cu species not only induced the formation of hollow Co/Cu-glycerate nanospheres from solid Co-glycerate nanospheres but also greatly enhanced the lithium storage performance of the Co/Cu-glycerate derived Co_3O_4/CuO. When examined as LIB anode, the optimized Co_3O_4/CuO hollow heterostructure displayed excellent lithium storage performance with high specific capacity (1156 mAh/g at 0.2 A/g), superior rate performance and outstanding cycling stability (930 mAh/g after 300 cycles at 0.5 A/g and 650 mAh/g after 500 cycles even at 2.0 A/g). Electrochemical analyses revealed that the Co_3O_4/CuO heterostructure demonstrated the synergistic enhancement effect with higher charge transfer rate and faster reaction kinetics as compared with the bare Co_3O_4 and CuO counterparts, while the unique hollow spherical structure exhibited robust structural stability and effectively buffered the volume changes upon lithiation/delithiation cycling. More importantly, we developed a novel synthetic strategy to fabricate well-defined hollow spherical metal glycerates/oxides, which can be promising for the development of high-performance electrode materials for energy-related applications.

Declaration of competing interest

The authors declare that they have no known competing financial interests or personal relationships that could have appeared to influence the work reported in this paper.

Acknowledgment

This work was supported by the National Natural Science Foundation of China (No. 52077175).

Supplementary materials

Supplementary material associated with this article can be found, in the online version, at doi:10.1016/j.cclet.2023.108450.

References

[1] N. Nitta, F. Wu, J.T. Lee, G. Yushin, Mater. Today 18 (2015) 252–264.
[2] A. Magasinski, P. Dixon, B. Hertzberg, et al., Nat. Mater. 9 (2010) 353–358.
[3] H. Wang, X. Yang, Q. Wu, et al., ACS Nano 12 (2018) 3406–3416.
[4] H. Wang, R. Qian, Y. Cheng, et al., J. Mater. Chem. A 8 (2020) 18425–18463.
[5] H. Wang, J. Wang, D. Cao, et al., J. Mater. Chem. A 5 (2017) 6817–6824.
[6] H. Shuai, R. Liu, W. Li, et al., Adv. Energy Mater. 13 (2022) 2202992.
[7] J. Xu, Q. Liu, Z. Dong, et al., ACS Appl. Mater. Interfaces 13 (2021) 54974–54980.
[8] Z.S. Wu, W. Ren, L. Wen, et al., ACS Nano 4 (2010) 3187–3194.
[9] Y. Xu, Q. Liu, Y. Zhu, et al., Nano Lett. 13 (2013) 470–474.
[10] J.W. Choi, D. Aurbach, Nat. Rev. Mater. 1 (2016) 16013.
[11] P. Roy, S.K. Srivastava, J. Mater. Chem. A 3 (2015) 2454–2484.
[12] J. Xu, S. Zhang, Z. Wei, et al., J. Colloid Interf. Sci. 585 (2021) 12–19.
[13] H.B. Wu, J.S. Chen, H.H. Hng, X.W. Lou, Nanoscale 4 (2012) 2526–2542.
[14] J. Zhu, T. Zhu, X. Zhou, et al., Nanoscale 3 (2011) 1084–1089.
[15] F.M. Courtel, H. Duncan, Y. Abu-Lebdeh, I.J. Davidson, J. Mater. Chem. 21 (2011) 10206–10218.
[16] X. Wang, X.L. Wu, Y.G. Guo, et al., Adv. Funct. Mater. 20 (2010) 1680–1686.
[17] D. Gu, W. Li, F. Wang, et al., Angew. Chem. Int. Ed. 54 (2015) 7060–7064.
[18] O. Waser, M. Hess, A. Güntner, P. Novák, S.E. Pratsinis, J. Power Sources 241 (2013) 415–422.
[19] Y. Pan, Y. Li, J. Song, et al., Appl. Surf. Sci. 601 (2022) 154273.
[20] W.L. Yao, J.L. Wang, J. Yang, G.D. Du, J. Power Sources 176 (2008) 369–372.
[21] J. Wang, L. Zhu, F. Li, et al., Small 16 (2020) e2002487.
[22] H. Wang, A.L. Rogach, Chem. Mater. 26 (2014) 123–133.
[23] D. Qian, Y. Gu, Y. Chen, et al., Mater. Lett. 238 (2019) 102–106.
[24] Y. Ji, J. Song, Y. Li, et al., Ceram. Int. 48 (2022) 15252–15260.
[25] Y. Kang, Y.H. Zhang, Q. Shi, et al., J. Colloid Interf. Sci. 585 (2021) 705–715.
[26] P. Zhang, J. Li, J. Feng, et al., Chin. Chem. Lett. 32 (2021) 2438–2442.
[27] M. Wu, H. Chen, L.P. Lv, Y. Wang, Chem. Engin. J. 373 (2019) 985–994.
[28] J. Wang, Q. Zhang, X. Li, et al., Nano Energy 6 (2014) 19–26.
[29] C. Yuan, L. Yang, L. Hou, et al., Energy Environ. Sci. 5 (2012) 7883–7887.
[30] W. Hao, S. Chen, Y. Cai, et al., J. Mater. Chem. A 2 (2014) 13801–13804.
[31] L. Shi, C. Fan, X. Fu, et al., Electrochim. Acta 197 (2016) 23–31.
[32] H. Wang, X. Lu, J. Tucek, et al., Electrochim. Acta 211 (2016) 636–643.
[33] F. Liao, X. Han, Y. Zhang, C. Xu, H. Chen, Ceram. Int. 44 (2018) 22622–22631.
[34] R. Atchudan, T.N.J.I. Edison, D. Chakradhar, et al., Ceram. Int. 44 (2018) 2869–2883.
[35] Z. Zhu, C. Han, T.-T. Li, et al., CrystEngComm 20 (2018) 3812–3816.
[36] Y. Tong, H. Liu, M. Dai, L. Xiao, X. Wu, Chin. Chem. Lett. 31 (2020) 2295–2299.
[37] Z. Wang, Y. Zhang, H. Xiong, et al., Sci. Rep. 8 (2018) 6530.
[38] C. Jiang, S. Liu, Q. Lian, et al., Ceram. Int. 43 (2017) 11354–11360.
[39] A. Shanmugavani, R.K. Selvan, Electrochim. Acta 188 (2016) 852–862.
[40] Y.J. Mai, X.L. Wang, J.Y. Xiang, et al., Electrochim. Acta 56 (2011) 2306–2311.
[41] G. Li, B. He, M. Zhou, et al., Ionics (Kiel) 23 (2016) 607–616.
[42] Y. Xu, K. Chu, Z. Li, et al., Dalton Trans. 49 (2020) 11597–11604.
[43] A.K. Rai, L.T. Anh, J. Gim, et al., J. Power Sources 244 (2013) 435–441.
[44] H. Yu, H. Fan, X. Wu, et al., Energy Storage Mater. 4 (2016) 145–153.
[45] A. Tomar, J. Singh, S.P. Singh, A.K. Rai, Physica E: Low-dimen. System. Nanostruct. 116 (2020) 113736.
[46] S. Sun, Z. Wen, J. Jin, Y. Cui, Y. Lu, Microporous Mesoporous Mater 169 (2013) 242–247.
[47] X. Yang, J. Zhang, Z. Wang, et al., Small 14 (2018) 1702669.
[48] L. Zhu, H. Lu, F. Xiao, et al., ACS Appl. Energy Mater. 3 (2020) 10215–10223.
[49] H. Kim, W. Choi, J. Yoon, et al., Chem. Rev. 120 (2020) 6934–6976.
[50] B. Wu, Y. Xie, Y. Meng, et al., J. Mater. Chem. A 7 (2019) 6149–6160.
[51] M. Jing, M. Zhou, G. Li, et al., ACS Appl. Mater. Interfaces 9 (2017) 9662–9668.
[52] T. Zheng, G. Li, X. Meng, S. Li, M. Ren, Chemistry 25 (2019) 885–891.